



HAL
open science

Electrical conductivity of omphacite and garnet indicates limited deep water recycling by crust subduction

Hanyong Liu, Kai Zhang, Jannick Ingrin, Xiaozhi Yang

► To cite this version:

Hanyong Liu, Kai Zhang, Jannick Ingrin, Xiaozhi Yang. Electrical conductivity of omphacite and garnet indicates limited deep water recycling by crust subduction. *Earth and Planetary Science Letters*, 2021, 559, pp.116784. 10.1016/j.epsl.2021.116784 . hal-03134606

HAL Id: hal-03134606

<https://hal.univ-lille.fr/hal-03134606>

Submitted on 8 Feb 2021

HAL is a multi-disciplinary open access archive for the deposit and dissemination of scientific research documents, whether they are published or not. The documents may come from teaching and research institutions in France or abroad, or from public or private research centers.

L'archive ouverte pluridisciplinaire **HAL**, est destinée au dépôt et à la diffusion de documents scientifiques de niveau recherche, publiés ou non, émanant des établissements d'enseignement et de recherche français ou étrangers, des laboratoires publics ou privés.

1

2

3 **Electrical conductivity of omphacite and garnet indicates limited**
4 **deep water recycling by crust subduction**

5

6 Hanyong Liu¹, Kai Zhang¹, Jannick Ingrin², Xiaozhi Yang^{1*}

7

8

9

10 ¹ State Key Laboratory for Mineral Deposits Research, School of Earth Sciences and

11 Engineering, Nanjing University, Nanjing 210023, PR China

12 ² Univ.Lille, CNRS, INRAE, ENSCL, UMR 8207, UMET, Unité Matériaux et

13 Transformations, F 59000 Lille, France

14

15

16

17 * Corresponding Author (xzyang@nju.edu.cn)

18

19 **Abstract**

20 It is usually stated that oceanic crust recycling at subduction zones introduces large
21 quantities of water into Earth's interior. However, it remains clouded how much water
22 is recycled to the deep mantle. This is largely due to the challenge in directly sampling,
23 and analyzing the water content of, a deep subducting crust. The subducting crust below
24 ~30 km depth is dominated by omphacite and garnet in eclogite-facies rocks. Here we
25 have determined the electrical conductivity of omphacite and garnet in representative
26 subduction-related eclogites, each with varying contents of Fe and H₂O that are key in
27 electrical conduction. Considering the measured conductivity, the eclogite chemistry by
28 geochemical investigations and the highly resistive property of subducting crusts by
29 geophysical surveys, we demonstrate that, at 70-120 km depths in the subducting crust,
30 the H₂O contents of omphacite and garnet are strikingly small, with the maximum value
31 being <400 and <80 ppm in the former and latter, respectively. The very small water
32 contents indicate extremely water-poor conditions, or very low water activity, during
33 the eclogite-facies metamorphism and in the system. This further implies the absence
34 of appreciated amounts of hydrous phases such as amphibole and chlorite in the matrix,
35 because of the strong ability of omphacite and garnet in hosting water as documented
36 in natural samples. We suggest that the recycling of water to the deep mantle by oceanic
37 crust subduction is limited. The results are important for modeling the conductivity of
38 subducting slabs and understanding the deep water circulation.

39

40 **1. Introduction**

41 The transport of water from the hydrosphere to the mantle plays a critical role in
42 affecting mantle dynamics, magma genesis and Earth's habitability. Water is recycled
43 back to the mantle by slab subduction. At very shallow depths (e.g., <20 km), the input

44 of water into the mantle is primarily controlled by pore water (Peacock, 1990; Cai et
45 al., 2018). In a downgoing slab at greater depths, however, water chiefly occurs as OH
46 groups bound in the structure of the constitutive minerals, both hydrous and nominally
47 anhydrous, note that H₂ dissolution in minerals is significant only at very high pressure
48 and reducing conditions (Yang et al., 2016). As a slab descends, water is gradually lost
49 by the breakdown of hydrous minerals such as amphibole and chlorite at depths mostly
50 <100 km, due to their instabilities at high temperature (Peacock, 1990; Liu et al., 1996;
51 Frost, 2006; Schmidt and Poli, 2014). Driven by its low density, the released water rises,
52 metasomatizes wallrocks and causes melting in the wedge. This causes the development
53 and widespread distribution of subduction zone volcanism and ore deposits.

54 It is widely believed that the crust layer in the slab is important for water recycling,
55 because most of the slab water is initially stored there (Ito et al., 1983; Peacock, 1990;
56 Dixon et al., 2002; Van Keken et al., 2002; Schmidt and Poli, 2014). Beyond ~30 km
57 depth, the slab crust is dominated by eclogites (via phase change), consisting mainly of
58 nominally anhydrous omphacite and garnet that are the main water carriers in eclogites
59 after hydrous minerals decompose (Lu and Keppeler, 1997; Bromiley and Keppeler, 2004;
60 Schmidt and Poli, 2014). As such, the water contents of omphacite and garnet are key
61 to understanding water recycling to the deep mantle. Omphacite and garnet in terrain
62 eclogites, that were once subducted to mantle depths and then returned to surface, could
63 hold up to several thousands of ppm H₂O as structural OH, leading to the suggestion
64 that the subducting crust is able to carry large quantities of water into the deep mantle
65 beyond the stability of the hydrous phases (Katayama and Nakashima, 2003; Katayama
66 et al., 2006; Sheng et al., 2007). The high water contents of omphacite and garnet in the
67 eclogites may, however, have suffered from complex secondary fluid-rock interactions
68 postdating eclogite peak-metamorphism (e.g., Sheng et al., 2007; Schmädicke and Gose,

69 2017). It is thus obscure how much water is present in omphacite and garnet in the deep
70 subducting crust.

71 The electrical conductivity of nominally anhydrous minerals (NAMs) is sensitive
72 to water (Karato, 1990; Dai and Karato, 2009; Yoshino et al., 2009; Yang et al., 2011,
73 2012; Yang and McCammon, 2012; Zhang et al., 2012, 2019; Zhao and Yoshino, 2016;
74 Liu et al., 2019). Meanwhile, electromagnetic surveys offer a direct window into Earth's
75 interior. In this context, constraints can be provided on the water contents of omphacite
76 and garnet in the subducting crust (and water recycling), if the conductivity structure of
77 subducting crusts is resolved and the electrical property of subduction-related materials
78 is determined. In a recent work, Liu et al. (2019) have quantified the effect of water on
79 the conductivity of omphacite and garnet, and provided a preliminary constraint on the
80 likely water content in the subducting crust. However, Liu et al. have not evaluated the
81 effect of Fe, which along with H are crucial in electrical conduction, and the question
82 arises how convincing their results might be applied to Earth's interior. In this report,
83 we have by experimental work measured the conductivity of omphacite and garnet from
84 representative eclogites, which plus the samples of Liu et al. (2019) show a wide range
85 of contents in Fe and H₂O. The data are used to infer the water contents of the minerals
86 in the subducting crust, by combining with geophysically-based electrical structure and
87 slab petrology. The results demonstrate clearly that a small amount of water is present
88 in omphacite and garnet in deep subducting crusts.

89 **2. Experiments and Methods**

90 **2.1 Starting materials and sample characterization**

91 Three starting eclogites were from Bixiling (omp1 + grt1) and Shuanghe (omp3 +
92 grt3) in China and Weißenstein (omp2 + grt2) in Germany, and were all related to slab
93 subduction and exhumation (Franz et al., 1986; Sheng et al., 2007). The Weißenstein

94 eclogite was studied in Liu et al. (2019). These samples were chosen by considering Fe
95 contents of constituting omphacite and garnet and quality of grains from >30 eclogites
96 (*note*: the electrical property of silicates is independent of the origin). Natural eclogites
97 were not used for conductivity studies directly, because of the occurrence of accessory
98 materials (e.g., secondary hydrous phases, fluid inclusions and/or other impurities) and
99 zoned water distribution that affect conductivity analyses. We analyzed the conductivity
100 of omphacite and garnet separately and then modeled the bulk conductivity. Omphacite
101 and garnet are representative in composition, in particular in Fe that almost covers the
102 content ranges in subduction-involved eclogites (omp1 and omp3: Appendix).
103 Optically clear omphacite/garnet grains, ~100-700 μm in size, were handpicked under
104 a binocular microscope. Each sample is chemically homogeneous in major-/minor-
105 elements (Table 1), as measured by a JEOL JXA-8230 electron microprobe (15 kV
106 accelerating voltage, 10 nA current and <5 μm beam size). Grains were ground to
107 powder, mostly 30-80 μm , and H-annealed with minor distilled water in Ni capsules
108 (ID 4.2 mm, OD 5.0 mm and length 10 mm) at 1-3.5 GPa and 650-700 $^{\circ}\text{C}$ (150-180 h
109 duration) in a piston cylinder press. By this, water homogenization was achieved in
110 each sample, and samples with different water contents were prepared. Dry samples
111 were not prepared, because OH is common in natural omphacite and garnet. Recovered
112 samples were cored into cylinders of 3 mm diameter and 1.7 mm length for subsequent
113 conductivity runs, note that the conductivity of silicate minerals by lattice conduction
114 is independent of grain size above ~5 μm that is typical for minerals in the deep Earth
115 (Yang and Heidelbach, 2012).

116 A precise analysis of water content is key for evaluating its effect on conductivity.
117 The general principle for water quantification in silicate minerals by Fourier-transform
118 infrared (FTIR) spectroscopy is given by the modified Beer-Lambert law: $C_{\text{H}} = Ab_{\text{S}_{\text{total}}}/I$,

119 where C_H is OH content, Abs_{total} is the total OH integrated absorbance normalized to 1
120 cm thickness, and I is the mineral-specific integral molar absorption coefficient. As
121 such, C_H is determined by Abs_{total} , once the coefficient I is externally calibrated. For
122 optically anisotropic minerals, the intensity of OH bands is sensitive to the orientation
123 of the IR active dipole relative to incident beam, and Abs_{total} is the sum of thickness-
124 normalized integrated absorbance along the three principal axes (a , b and c). This
125 requires orienting samples and polarized FTIR analyses along the axes, which are
126 difficult for small grains and are time-consuming for sample preparation. Recently,
127 Shuai and Yang (2017) have shown that Abs_{total} can be well characterized by polarized
128 FTIR analyses along any three mutually perpendicular directions of a given sample,
129 without the necessity to orient the samples; in case very small grains which are unable
130 to be prepared for polarized FTIR work, Qiu et al. (2018) have demonstrated that Abs_{total}
131 can be obtained by unpolarized FTIR analyses on randomly oriented grains.

132 Water contents were measured by a Bruker Vertex 70V FTIR spectrometer coupled
133 with a Hyperion 2000 microscope. Analyses were performed on optically clear grains
134 with an aperture of $60 \times 60 \mu\text{m}$ and a resolution of 4 cm^{-1} (128 scans for each spectrum
135 by a globar source, KBr-Ge beam splitter, MCT detector and wire-grid Ze-Se polarizer).
136 For anisotropic omphacite, polarized spectra were acquired for relatively large grains
137 in annealed samples before conductivity runs (Shuai and Yang, 2017), and unpolarized
138 spectra on 15-20 randomly oriented grains were obtained for fine-grained samples after
139 conductivity runs (Qiu et al., 2018). For cubic garnet, unpolarized spectra were recorded
140 over 6-9 grains. Water contents were calibrated by the mineral-specific coefficients of
141 Katayama et al. (2006) for omphacite and garnet in eclogites, and uncertainty is mostly
142 $<10\%$, as documented in Shuai and Yang (2017) and Qiu et al. (2018). For a comparison
143 under the same framework, the same calibration was used to recalculate the H_2O content

144 of minerals in natural eclogites in available studies. This yields values different from
145 some early work, e.g., the 1840 ppm OH of omphacite in Smyth et al. (1991), estimated
146 by the OH peak linear intensity, is actually ~310 ppm H₂O; in contrast, the H₂O contents
147 of omphacite and garnet in recent reports (Katayama and Nakashima, 2003; Katayama
148 et al., 2006; Sheng et al., 2007; Schmädicke and Gose, 2017) are less affected. The
149 general results of this work are not affected by adopting the calibration coefficients.

150 **2.2 Conductivity experiments at elevated conditions**

151 Slabs are rather oxidizing above ~200 km depth, with redox state similar to the Ni-
152 NiO buffer (McCammon, 2005). Therefore, conductivity runs were carried out with Ni-
153 NiO at 1-2.5 GPa and 250-850 °C in an end-loaded piston cylinder press. The assembly
154 design resembles that in our previous studies (Yang et al., 2011, 2012; Yang, 2012; Yang
155 and Heidelbach, 2012; Yang and McCammon, 2012; Li et al., 2016, 2017; Liu et al.,
156 2019), and only a brief description is offered. In each run, a BN-Ni double capsule was
157 adopted to maintain sample geometry and yield a relatively sealed chamber. BN causes
158 reducing conditions only when O₂ is rich (e.g., in air) and run duration is long above
159 ~1000 °C, by $4\text{BN} + 3\text{O}_2 = 2\text{B}_2\text{O}_3 + 2\text{N}_2$, and BN itself in a sealed system does not
160 influence the redox state. It has been demonstrated that, for the design at <1000 °C and
161 short duration (typical of conductivity runs), the reaction of Pt and Fe in samples is
162 negligible and the redox state in the chamber is well buffered, as tested with pyroxenes
163 and olivine (Yang et al., 2011, 2012; Yang, 2012; Yang and McCammon, 2012).

164 Before assembly, Al₂O₃ parts were heated at 1000 °C to remove absorbed water,
165 and during assembly, no cement/glue was used to immobilize the various parts to avoid
166 volatile release at high temperature that affects the analyses. Completed assembly was
167 heated at 136 °C overnight, and was heated again at 200 °C after loading into the press.
168 Impedance spectra were recorded in the heating-cooling cycles, with a Solartron 1260

169 Impedance/Gain Phase analyser by frequency sweeping at 10^6 -1 Hz and 0.5 V applied
170 voltage. Temperature of the analyses was up to 850 °C, to minimize water diffusion loss
171 of samples upon heating. Duration was typically ~1 min or less per analysis (depending
172 on temperature). After each run, recovered capsule was polished for optical, FTIR and
173 backscattered electron examinations. Ni-NiO pairs were present, and sample distortions
174 and grain growths were negligible, as observed in similar work (Yang et al., 2011, 2012;
175 Yang, 2012; Yang and Heidelbach, 2012; Yang and McCammon, 2012; Li et al., 2017;
176 Liu et al., 2019). Resistance (R) was obtained from the impedance spectra (see below),
177 and conductivity (σ) was calculated by $\sigma = L/SR$, where L and S are the effective sample
178 length and cross-section area, respectively. Uncertainty is usually <5% for conductivity
179 and <20 °C for temperature.

180 **3. Results**

181 Representative FTIR spectra of annealed samples are shown in Fig. 1. The spectra
182 show absorption peaks at 3610-3625, 3500-3520 and 3440-3460 cm^{-1} in the omphacites
183 and at 3610-3640 and 3530-3550 cm^{-1} in the garnets, which are typical of OH bands in
184 the eclogite minerals (Smyth et al., 1991; Katayama and Nakashima, 2003; Katayama
185 et al., 2006; Sheng et al., 2007; Schmädicke and Gose, 2017). In each mineral, the peak
186 frequency positions are similar, suggesting similar H incorporation mechanism, and the
187 relative difference of peak intensity between different samples are due to different water
188 contents and/or grain orientations. Sample H_2O contents are basically the same prior to
189 and after each conductivity run (Table 2). Fe and other major-/minor-elements are more
190 sluggish than H, and their contents are unchanged in the runs. Representative complex
191 spectra are presented in Fig. 2. The spectra usually show a high frequency arc and a low
192 frequency tail, although the tail is sometimes not obvious, and the spectral shapes are
193 similar to those reported for other minerals (Dai and Karato, 2009; Yoshino et al., 2009;

194 Yang et al., 2011, 2012; Yang, 2012; Zhang et al., 2012, 2019; Zhao and Yoshino, 2016;
195 Li et al., 2016, 2017; Liu et al., 2019). The arc and tail was by sample lattice conduction
196 and electrode effects, respectively.

197 The conductivity of NAMs (and other Earth materials) is quantitatively described
198 by the Arrhenius relation:

$$\sigma = \sigma_0 \cdot \exp(-\Delta H / RT) \quad (1)$$

199 where σ_0 is a constant, ΔH is the activation enthalpy, R is the ideal gas constant, and T
200 is temperature. Conductivities in the first heating were sometimes affected by residual
201 moisture in the chamber, yielding data not obeying Eq. (1) as observed in similar studies
202 (Yang et al., 2012; Yang and Heidelbach, 2012; Li et al., 2017; Liu et al., 2019), and the
203 influenced data were excluded. Conductivity data and the fittings to Eq. (1) are shown
204 in Fig. 3, and fit parameters are given in Table 2. Sample conductivity is much greater
205 than the assembly background conductivity (Yang et al., 2011). The data are consistent
206 between different heating-cooling cycles in each run (see also Appendix), suggesting
207 the absence of system hysteresis. The conductivity is slightly larger at 2.5 than at 1 GPa,
208 indicated by the runs with an OH-bearing omphacite (omp3). This is consistent with
209 the previous study on an OH-bearing pyrope that shows similar conductivity
210 enhancement by pressure (Dai and Karato, 2009). In contrast, the conductivity of dry
211 olivine or garnet decreases slightly with increasing pressure (Xu et al., 2000; Dai and
212 Karato, 2009). The difference is caused by the different pressure dependence between
213 small polaron and H conduction in the minerals (see Section 4), but the effect of
214 pressure (at a small variation) on the conductivity of silicate minerals is in general
215 insignificant.

216 **4. Fe- and H-dependent conductivity**

217 In Fe- and H-bearing NAMs, the conductivity is related to the conduction of small

218 polarons (electron-hole hopping between Fe^{2+} and Fe^{3+}) and protons (H). Our data show
219 that, at otherwise identical conditions, the conductivity of both omphacite and garnet
220 increases with Fe and H_2O contents (Fig. 3), agreeing with studies on other NAMs (Dai
221 and Karato, 2009; Yoshino et al., 2009; Yang et al., 2011, 2012; Yang and McCammon,
222 2012; Zhang et al., 2012; Zhao and Yoshino, 2016). The data trends of our omphacites
223 are consistent with those of synthetic omphacites at 3 GPa (Zhang et al., 2019), and the
224 conductivity of the omphacite (omp3) with 7.92 wt.% FeO and 70 ppm H_2O is close to
225 that of an augite with 8.31 wt.% FeO and 75 ppm H_2O at 1 GPa (Yang and McCammon,
226 2012) (Fig. 3a). The conductivity of the omphacite (omp1) with 1.46 wt.% and 200 ppm
227 H_2O resembles that of the one (omp2) with 4.27 wt.% and 150-290 ppm H_2O , implying
228 an insignificant effect of Fe at that content range. At a similar 155-160 ppm H_2O , the
229 conductivity of the Fe-rich garnet (15.40 wt.% FeO) is less than that reported by Dai
230 and Karato (2009) for a Fe-poor pyrope (7.42 wt.% FeO) at 8 GPa (Fig. 3b). Probably,
231 this is related to the different pressures (1 vs. 8 GPa) and H-species (note that different
232 H-defects could have different mobility, contributing differently to the conduction), e.g.,
233 narrow OH bands at $3700\text{-}3500\text{ cm}^{-1}$ in this study vs. broad bands at $3800\text{-}3000\text{ cm}^{-1}$ in
234 Dai and Karato (2009). The conductivity of our garnets is close at similar contents of
235 FeO (26.55-26.58 wt.%) and H_2O (100-110 ppm, with similar OH band shapes, Fig. 1).
236 The activation enthalpy is Fe-dependent in omphacite, ~ 87 , 81-84 and 65 kJ/mol at 1.64,
237 4.27 and 7.92 wt.% FeO, respectively, but is broadly Fe-independent in garnet, 88-91
238 kJ/mol over a large range of Fe contents, 15.40-26.58 wt.% FeO (Table 1). Therefore,
239 the effect of Fe on the conductivity of omphacite and garnet is mineral dependent.

240 For the same omphacite or garnet in eclogite samples under similar conditions, the
241 conductivity is linearly proportional to water content below $\sim 1000\text{ }^\circ\text{C}$ and at moderate
242 H_2O contents (Liu et al., 2019; Zhang et al., 2019). This has also been reported for many

243 other NAMs such as augite, diopside, enstatite, plagioclase, pyrope and olivine (Yang
 244 et al., 2011, 2012; Yang and McCammon, 2012; Zhang et al., 2012; Zhao and Yoshino,
 245 2016). For an OH-bearing mineral with a fixed content of Fe (and other major elements),
 246 the relative contribution of small polaron conduction is usually much smaller than that
 247 of proton conduction at relatively low temperature. Eq. (1) can be approximated by:

$$\sigma \propto C_H \cdot \exp(-\Delta H_H / RT) \quad (2)$$

248 where ΔH_H is the activation enthalpy by H conduction and is numerically equal to ΔH
 249 in Eq. (1). As such, the conductivity of both omphacite and garnet can be modeled for
 250 a range of H₂O contents at each of the starting FeO contents (Fig. 4). The essentially
 251 same conductivity of omphacite with 1.64 and 4.27 wt.% FeO at the same H₂O content,
 252 as noted above, indicates a more significant role of H than Fe at such Fe content levels.
 253 The N-type semiconductor relation is used to model the effect of both Fe and H on the
 254 conductivity of both minerals:

$$\sigma = A \cdot X_{Fe}^n \cdot C_H \cdot \exp[-(\Delta E - \alpha X_{Fe}^{1/3} - \beta C_H^{1/3}) / RT] \quad (3)$$

255 where X_{Fe} is the molar fraction of Fe (= Fe/(Fe + Mg)), ΔE is the activation energy, and
 256 A , n , α and β are constants. The insensitivity of omphacite conductivity to FeO content
 257 at 1.64-4.27 wt.% makes it hard to model the whole dataset with Eq. (3). In this context,
 258 the modeling is carried out for omphacite using the conductivity data of our samples
 259 starting with omp1 and omp3, that restrict the boundaries of Fe contents in subduction-
 260 related omphacites, and the synthetic omphacite (5.81 wt.% FeO and 420 ppm H₂O
 261 with similar OH band positions) of Zhang et al. (2019), and for garnet using the data of
 262 all our samples (the Dai and Karato (2009) pyropes are not used because of the different
 263 OH bands). This yields ΔE , A , n , α and β of 106 ± 6 kJ/mol, 2754 ± 380 S/m, -0.05 ± 0.09 ,
 264 64 ± 6 kJ/mol and -26 ± 8 kJ/mol for omphacite, and 89 ± 3 kJ/mol, 61660 ± 4085 S/m,
 265 4.25 ± 1.32 , -4 ± 31 kJ/mol and 15 ± 9 kJ/mol for garnet. For both minerals, the modeled

266 results by Eq. (2) and (3) are well consistent at the same H₂O and boundary Fe contents,
267 especially at >500 °C (Fig. 4).

268 The bulk conductivity of eclogite is calculated from omphacite and garnet with the
269 Hashin and Shtrikman (1962) bounds, which offer the narrowest restrictions of a two-
270 phase composite despite the geometrical configurations:

$$\begin{aligned}\sigma_{HS+} &= \sigma_1 + x_2[(\sigma_2 - \sigma_1)^{-1} + x_1 / (3\sigma_1)]^{-1} \\ \sigma_{HS-} &= \sigma_2 + x_1[(\sigma_1 - \sigma_2)^{-1} + x_2 / (3\sigma_2)]^{-1}\end{aligned}\quad (4)$$

271 where σ_{HS+} and σ_{HS-} are the upper and lower bounds, respectively, given $\sigma_1 > \sigma_2$ (x is the
272 volume proportion). A key prerequisite for the modeling is the equilibrium distribution
273 of major/minor elements and OH between coexisting minerals. This is a factor that must
274 be considered when modeling the bulk conductivity of any matrix consisting of several
275 phases. The calculation is carried out by Eq. (2) using the conductivity data of minerals
276 at different H₂O contents for each starting Fe content, in which case the effect of Fe is
277 constrained at the same time (Fig. 4). Eq. (3) is not adopted, because of the difficulty in
278 controlling chemical equilibrium between the two minerals. Each of the mineral pairs,
279 omp1-grt1, omp2-grt2 and omp3-grt3, was separated from the same starting eclogite,
280 and the major/minor elements are already in equilibrium. The water partition coefficient
281 between omphacite and garnet in eclogite, ~0.2 from Katayama et al. (2006), is adopted
282 to obtain the equilibrium H₂O contents (assuming 100, 200 and 400 ppm in omphacite).
283 The bulk conductivity of eclogite is not affected by likely minor impurities, because if
284 present, they are usually isolated (not connected) in the matrix and do not contribute to
285 bulk conduction. The results are shown in Fig. 5a and b for omphacite-rich and garnet-
286 rich rocks, respectively. This produces the modeled bulk conductivity at variable Fe and
287 H₂O contents and high temperature. In particular, The FeO contents reflect the range of
288 the two minerals in subducting crusts (as noted before). Given other conditions, σ_{HS+}

289 and σ_{HS} of each sample show a small variation above 600 °C, and are up to ~0.1 S/m
290 at 900 °C (for the modeled composition). Considering the positive pressure effect on
291 the conductivity of OH-bearing omphacite and garnet as mentioned above, the bulk
292 conductivity is only slightly greater at higher pressure.

293 **5. Water contents in subducting omphacite and garnet**

294 Electromagnetic induction is sensitive to conductive rather than resistive bodies in
295 Earth's interior. This makes it hard to accurately resolve the conductivity of subducting
296 crusts that are highly resistive. Usually, high conductivity is not detected in subducting
297 slabs, and slab conductivity is much smaller than that of mantle wedge and surrounding
298 mantle in the inversion results. Conductivity of the subducting crust, either fast or slow
299 subduction in diverse settings, is estimated to be mostly 10^{-4} to 10^{-3} S/m at ~70-120 km
300 depth (Vanyan et al., 2002; McGary et al., 2014; Ichiki et al., 2015; Vargas et al., 2019).
301 This is a reasonable estimate by imposing a 1000, 5000 or 10000 Ω slab resistivity in
302 the inversion models (Ichiki et al., 2015). A typical electrical structure of a subducting
303 crust is given in Fig. 5c (after McGary et al. (2014) who focused on conductive channels
304 in the wedge). We want to note that, although Evans et al. (2014) have offered a variety
305 of outputs (mainly in the wedge) with the same electromagnetic data of McGary et al.
306 (2014) by applying different inversion methods, the crust portion at ~70-120 km depth
307 is very resistive in most of their models. Moreover, Fig. 5c is for the Cascadia area, but
308 broadly similar results on resistive slab vs. depth have been reported for other tectonic
309 environments (e.g., Vanyan et al., 2002; Ichiki et al., 2015; Vargas et al., 2019).

310 It has been shown that, despite a wide range of ages, geometries and convergence
311 rates, slabs actually share many common features with their thermal structures (Peacock,
312 1996; Syracuse et al., 2010; Penniston-Dorland et al., 2015). At ~70-120 km depth, the
313 temperature is mostly ~600-900 °C in the crust layer, for subduction zones over various

314 tectonic settings. The FeO content is ~1-8 wt.% of omphacite and 14-27 wt.% of garnet
315 in terrane eclogites that were once brought to ~200 km depth (Katayama and Nakashima,
316 2003; Katayama et al., 2006; Sheng et al., 2007; and Appendix), suggesting that deeply
317 subducting eclogites are in fact not depleted in Fe. As such, to cause the 10^{-4} - 10^{-3} S/m
318 conductivity of subducting crusts at ~600-900 °C, the only possibility is that omphacite
319 and garnet are water-poor. According to the modeling in Fig. 5a-b, the H₂O contents are
320 <400 ppm in omphacite and <80 ppm in garnet at 600 °C and <100 ppm in omphacite
321 and <20 ppm in garnet at 900 °C for the bottom Fe boundaries (omp1-grt1), and <30
322 ppm for the top Fe boundaries (omp3-grt3). These H₂O-content ranges are meaningful,
323 in particular if considering the weaker effect of a minor variation in Fe than in H content
324 (Section 4), and can be even smaller, if the effect of pressure on the conductivity of OH-
325 bearing omphacite and garnet is considered (Section 3). The maximum <400 ppm H₂O
326 content resembles that estimated in Liu et al. (2019), which is based on omp2 in contrast
327 to omp1 in this study (due to the more significant effect of H at the Fe content levels as
328 noted above). The inferred H₂O contents of omphacite and garnet in subducting crusts
329 (~70-120 km depth) are much less than those up to 2000-3000 ppm in terrane eclogites
330 (Katayama and Nakashima, 2003; Katayama et al., 2006). This suggests that OH-rich
331 omphacite and garnet in the terrane samples were H-enriched by secondary processes
332 during their exhumation to surface, in line with the arguments by analyzing mineral OH
333 patterns and D/H ratios (Sheng et al., 2007; Schmädicke and Gose, 2017). Interestingly,
334 the H₂O values resemble the mostly <360 ppm of omphacite and <65 ppm of garnet in
335 volcano-hosted xenolith eclogites (Smyth et al., 1991; Bell and Rossman, 1992; Koch-
336 Müller et al., 2004). This makes more sense if xenolith eclogites represent the various
337 dehydrated products of subducted crusts that were accidentally entrained by volcanoes
338 and transferred to the surface; however, things could be complicated because a general

339 consensus has not been reached for the origin of xenolith eclogites, e.g., some may form
340 by melt accumulation (Jacob, 2004).

341 Consequently, the conductivity data and inferred water contents of omphacite and
342 garnet are broadly consistent with the constraints from other approaches. The inversion
343 of electromagnetic data at subduction zones has long been subjected to the difficulty in
344 adopting a good reference resistor in the starting model. In most cases, the inversion is
345 carried out by highlighting the conductivity contrast between the resistive slab and the
346 conductive paths in the wedge (linked to melting and/or dehydrated fluids). In order to
347 identify fine-scale variation of conductivity in the subducting slab, e.g., due to change
348 of temperature and release of water with subduction, it is important to impose a reliable
349 slab conductivity in the inversion model. The water contents of minerals in the slab, the
350 electrical properties of eclogites and the conductivity laws, as provided here, allow to
351 model the conductivity of oceanic crusts as a function of temperature and water content
352 as the starting reference resistor for the inversion of electromagnetic data.

353 **6. Implications for deep water recycling**

354 The very low water contents of omphacite and garnet at ~70-120 km depth imply
355 a much smaller water content in the subducting crust than the original value dominated
356 by hydrous phases (e.g., amphibole and chlorite), e.g., ~1-2 wt.% H₂O (Peacock, 1990).
357 Water in the subducting crust is mostly released at shallow depths, and the dehydration
358 of hydrous phases and omphacite and garnet in eclogites produces conductive channels
359 in the wedge (McGary et al., 2014). Eclogite-facies metamorphism, which involves all
360 materials in the system, occurs at >30 km depths in the subducting crust (e.g., Peacock,
361 1990; Schmidt and Poli, 2014). The inferred small water contents of omphacite and
362 garnet are indicative of extremely water-poor conditions, or very low water activity,
363 during the metamorphism and in the system. Otherwise, the water contents of the two

364 minerals would dramatically increase, due to their strong ability in accommodating OH
365 (Katayama and Nakashima, 2003; Katayama et al., 2006; Sheng et al., 2007), and their
366 conductivity would be greatly enhanced, leading to conductive zones in the subducting
367 slab that is inconsistent with geophysical mappings (Vanyan et al., 2002; McGary et al.,
368 2014; Ichiki et al., 2015; Vargas et al., 2019). The water-poor conditions also imply
369 very minor to negligible amounts of hydrous phases in the system, because of their
370 extensive dehydration and water escape at shallow depths. This agrees with the
371 arguments that subducting crusts may contain no hydrous minerals beyond ~3 GPa and
372 700 °C, as advocated by considering dehydration in natural rocks, numerical modeling
373 and phase stabilities (Liu et al., 1996; Schmidt and Poli, 2014).

374 In this context, the amount of water carried to the deep mantle by subducting crust
375 is regulated by omphacite and garnet in eclogites, but not hydrous phases. This implies
376 a minor amount of water that could be brought to the deep mantle, although it might be
377 significant at very shallow depths (Peacock, 1990; Cai et al., 2018). Assuming the total
378 length, thickness and density of subducting oceanic crusts of 40000 km (Syracuse et al.,
379 2010), 6 km and 3 g/cm³, respectively, and the average rate of subduction of 5 cm/year,
380 the mass of water transferred to the mantle exceeding ~70 km depth in the past 3 billion
381 years would correspond to <3% of the oceans. A direct implication is that the exchange
382 of water between Earth's exterior and interior reservoirs might not be efficient. This fits
383 well with the high dehydration efficiency (>92%) of subducting crusts at shallow depths,
384 estimated from the H₂O/Ce ratios of mid-ocean ridge basalts (Dixon et al., 2002), and
385 the preservation of protosolar nebular water in the deep mantle over Earth's evolution,
386 constrained by the D/H ratios of plume-related lavas (Hallis et al., 2015). The limited
387 water transfer by crust deep subduction does not mean a water-poor deep Earth, because
388 surface water (and atmosphere) formed by degassing of the Earth (Allègre et al., 1987)

389 and its deep interior was already hydrous.

390 Consequently, the water flux into the deep mantle is much smaller than that simply
391 estimated from the stabilities of hydrous minerals such as amphibole, chlorite and dense
392 hydrous magnesium silicates, by assuming their continuous presence in appreciated
393 amounts in the downgoing crust. The stability fields of hydrous phases are established
394 by experiments at water saturated/super-saturated conditions, e.g., with up to >10 wt.%
395 water in sealed capsules (Liu et al., 1996; Frost, 2006; Schmidt and Poli, 2014). This
396 requirement is hard to always fulfil in the subducting crust that is not a closed system
397 and contains an initial H₂O content of ~1-2 wt.% prior to subduction (Peacock, 1990),
398 which is mostly released at shallow depths. Thus, there is a gap between the water-poor
399 state in the deep slab and the water-rich state in laboratory. Finally, if slab mantle bears
400 serpentine, e.g., by the serpentinization of peridotites providing there is enough water
401 for serpentine formation prior to subduction, then its role in conveying water to Earth's
402 interior should be evaluated. Key to this issue is to map the actual amount of serpentine
403 in the slab mantle and the dynamics of the low density with subduction, e.g., 2.6 g/cm³
404 of serpentine vs. 3.4 g/cm³ of peridotite and 3.6 g/cm³ of eclogite. This is beyond the
405 scope of this work, and more studies are required.

406 **Acknowledgements**

407 We thank Lingmin Zhang for assistance with microprobe analyses and Charles Geiger
408 for some text polishing on an early version. X.Y. is deeply indebted to Masahiro Ichiki
409 and Philip Wannamaker for clarifying the electrical structure of subducting slab and the
410 technical issues of electromagnetic work. X.Y. thanks Joseph Smyth and Monika Koch-
411 Müller for discussions. Editorial handling by James Badro and comments by Fabrice
412 Gaillard and one anonymous reviewer helped to improve the manuscript. This study
413 was supported by National Science Foundation of China (41725008) and National Key

414 R&D Program of China (2018YFA0702704).

415 **References**

- 416 Allègre, C.J., Staudacher, T., Sarda, P., 1987. Rare gas systematics: formation of the atmosphere,
417 evolution and structure of the Earth's mantle. *Earth Planet. Sci. Lett.* 81, 127–150.
- 418 Bell, D.R., Rossman, G.R., 1992. Water in Earth's mantle: the role of nominally anhydrous minerals.
419 *Science* 255, 1391–1397.
- 420 Bromiley, G.D., Keppler, H., 2004. An experimental investigation of hydroxyl solubility in jadeite
421 and Na-rich clinopyroxenes. *Contrib. Mineral. Petrol.* 147, 189–200.
- 422 Cai, C., Wiens, D.A., Shen, W., Eimer, M., 2018. Water input into the Mariana subduction zone
423 estimated from ocean-bottom seismic data. *Nature* 563, 389–392.
- 424 Dai, L., Karato, S.I., 2009. Electrical conductivity of pyrope-rich garnet at high temperature and
425 high pressure. *Phys. Earth Planet. Inter.* 176, 83–88.
- 426 Dixon, J.E., Leist, L., Langmuir, C.H., Schilling, J.G., 2002. Recycled dehydrated lithosphere
427 observed in plume-influenced mid-ocean-ridge basalt. *Nature* 420, 385–389.
- 428 Evans, R.L., Wannamaker, P.E., McGary, R.S., Elsenbeck, J., 2014. Electrical structure of the central
429 Cascadia subduction zone: The EMSLAB Lincoln Line revisited. *Earth Planet. Sci. Lett.* 402,
430 265–274.
- 431 Franz, G., Thomas, S., Smith, D.C., 1986. High-pressure phengite decomposition in the Weissens-
432 tein eclogite, Münchberger Gneiss Massif, Germany. *Contrib. Mineral. Petrol.* 92, 71–85.
- 433 Frost, D.J., 2006. The stability of hydrous mantle phases. *Rev. Mineral. Geochem.* 62, 243–271.
- 434 Hallis, L.J., Huss, G.R., Nagashima, K., Taylor, G.J., Halldórsson, S.A., Hilton, D.R., Mottl, M.J.,
435 Meech, K.J., 2015. Evidence for primordial water in Earth's deep mantle. *Science* 350, 795–797.
- 436 Hashin, Z., Shtrikman, S., 1962. A variational approach to the theory of the effective magnetic
437 permeability of multiphase materials. *J. Appl. Phys.* 33, 3125–3131.
- 438 Ichiki, M., Ogawa, Y., Kaida, T., Koyama, T., Uyeshima, M., Demachi, T., Hirahara, S., Honkura,
439 Y., Kanda, W., Kono, T., Matsushima, M., Nakayama, T., Suzuki, S., Toh, H., 2015. Electrical
440 image of subduction zone beneath northeastern Japan. *J. Geophys. Res.* 120, 7937–7965.
- 441 Ito, E., Harris, D.M., Anderson Jr, A.T., 1983. Alteration of oceanic crust and geologic cycling of
442 chlorine and water. *Geochim. Cosmochim. Acta* 47, 1613–1624.
- 443 Jacob, D.E., 2004. Nature and origin of eclogite xenoliths from kimberlites. *Lithos* 77, 295–316.
- 444 Karato, S., 1990. The role of hydrogen in the electrical conductivity of the upper mantle. *Nature*
445 347, 272–273.
- 446 Katayama, I., Nakashima, S., 2003. Hydroxyl in clinopyroxene from the deep subducted crust:
447 evidence for H₂O transport into mantle. *Am. Mineral.* 88, 229–234.
- 448 Katayama, I., Nakashima, S., Yurimoto, H., 2006. Water content in natural eclogite and implication
449 for water transport into the deep upper mantle. *Lithos* 86, 245–259.
- 450 Koch-Müller, M., Matsyuk, S., Wirth, R., 2004. Hydroxyl in omphacites and omphacitic
451 clinopyroxenes of upper mantle to lower crustal origin beneath the Siberian platform. *Am. Mineral.*
452 89, 921–931.
- 453 Li, Y., Yang, X., Yu, J.H., Cai, Y.F., 2016. Unusually high electrical conductivity of phlogopite: the
454 possible role of fluorine and geophysical implications. *Contrib. Mineral. Petrol.* 171:37,
455 10.1007/s00410-016-1252-x.
- 456 Li, Y., Jiang, H., Yang, X., 2017. Fluorine follows water: Effect on electrical conductivity of silicate
457 minerals by experimental constraints from phlogopite. *Geochim. Cosmochim. Acta* 217, 16–27.
- 458 Liu, J., Bohlen, S.R., Ernst, W.G., 1996. Stability of hydrous phases in subducting oceanic crust.
459 *Earth Planet. Sci. Lett.* 143, 161–171.
- 460 Liu, H., Zhu, Q., Yang, X., 2019. Electrical conductivity of OH-bearing omphacite and garnet in
461 eclogite: the quantitative dependence on water content. *Contrib. Mineral. Petrol.* 176: 57,
462 10.1007/s00410-019-1593-3.
- 463 Lu, R., Keppler, H., 1997. Water solubility in pyrope to 100 kbar. *Contrib. Mineral. Petrol.* 129, 35–
464 42.
- 465 McCammon, C., 2005. The paradox of mantle redox. *Science* 308, 807–808.
- 466 McGary, R.S., Evans, R.L., Wannamaker, P.E., Elsenbeck, J., Rondenay, S., 2014. Pathway from
467 subducting slab to surface for melt and fluids beneath Mount Rainier. *Nature* 511, 338–340.
- 468 Peacock, S.M., 1996. Thermal and petrologic structure of subduction zones. *Subduction Top Bottom*

469 96, 119–133.

470 Peacock, S.M., 1990. Fluid processes in subduction zones. *Science* 248, 329–337.

471 Penniston-Dorland, S.C., Kohn, M.J., Manning, C.E., 2015. The global range of subduction zone
472 thermal structures from exhumed blueschists and eclogites: Rocks are hotter than models. *Earth*
473 *Planet. Sci. Lett.* 428, 243–254.

474 Qiu, Y., Jiang, H., Kovacs, I., Xia, Q.-K., Yang, X., 2018. Quantitative analysis of H-species in
475 anisotropic minerals by unpolarized infrared spectroscopy: An experimental evaluation. *Am.*
476 *Mineral.* 103, 1761–1769.

477 Schmädicke, E., Gose, J., 2017. Water transport by subduction: clues from garnet of Erzgebirge
478 UHP eclogite. *Am. Mineral.* 102, 975–986.

479 Schmidt, M.W., Poli, S., 2014. Devolatilization During Subduction, in: *Treatise on Geochemistry*.
480 pp. 669–701.

481 Sheng, Y.M., Xia, Q.K., Dallai, L., Yang, X.Z., Hao, Y.T., 2007. H₂O contents and D/H ratios of
482 nominally anhydrous minerals from ultrahigh-pressure eclogites of the Dabie orogen, eastern
483 China. *Geochim. Cosmochim. Acta* 71, 2079–2103.

484 Shuai, K., Yang, X., 2017. Quantitative analysis of H-species in anisotropic minerals by polarized
485 infrared spectroscopy along three orthogonal directions. *Contrib. Mineral. Petrol.* 172, 14, doi:
486 10.1007/s00410-017-1336-2.

487 Smyth, J.R., Bell, D.R., Rossman, G.R., 1991. Incorporation of hydroxyl in upper-mantle
488 clinopyroxenes. *Nature* 351, 732–735.

489 Syracuse, E.M., van Keken, P.E., Abers, G.A., 2010. The global range of subduction zone thermal
490 models. *Phys. Earth Planet. Inter.* 183, 73–90.

491 Van Keken, P.E., Kiefer, B., Peacock, S.M., 2002. High-resolution models of subduction zones:
492 Implications for mineral dehydration reactions and the transport of water into the deep mantle.
493 *Geochem. Geophys. Geosyst.* 3, 10.1029/2001GC000256.

494 Vanyan, L.L., Berdichevsky, M.N., Pushkarev, P.Y., Romanyuk, T.V., 2002. A geoelectric model of
495 the Cascadia subduction zone. *Izv. Phys. Solid Earth* 38, 816–845.

496 Vargas, J.A., Meqbel, N.M., Ritter, O., Brasse, H., Weckmann, U., Yáñez, G., Godoy, B., 2019.
497 Fluid distribution in the Central Andes subduction zone imaged with magnetotellurics. *J. Geophys.*
498 *Res.* 124, 4017–4034.

499 Xu, Y., Shankland, T.J., Duba, A.G., 2000. Pressure effect on electrical conductivity of mantle
500 olivine. *Phys. Earth Planet. Inter.* 118, 149–161.

501 Yang, X., 2012. Orientation-related electrical conductivity of hydrous olivine, clinopyroxene and
502 plagioclase and implications for the structure of the lower continental crust and uppermost mantle.
503 *Earth Planet. Sci. Lett.* 317–318, 241–250.

504 Yang, X., Heidelberg, F., 2012. Grain size effect on the electrical conductivity of clinopyroxene.
505 *Contrib. Mineral. Petrol.* 163, 939–947.

506 Yang, X., Keppler, H., Li, Y., 2016. Molecular hydrogen in mantle minerals. *Geochem. Perspect.*
507 *Lett.* 2, 160–168.

508 Yang, X., Keppler, H., McCammon, C., Ni, H., 2012. Electrical conductivity of orthopyroxene and
509 plagioclase in the lower crust. *Contrib. Mineral. Petrol.* 163, 33–48.

510 Yang, X., Keppler, H., McCammon, C., Ni, H., Xia, Q., Fan, Q., 2011. The effect of water on the
511 electrical conductivity of lower crustal clinopyroxene. *J. Geophys. Res.* 116, B04208,
512 10.1029/2010JB008010.

513 Yang, X., McCammon, C., 2012. Fe³⁺-rich augite and high electrical conductivity in the deep
514 lithosphere. *Geology* 40, 131–134.

515 Yoshino, T., Matsuzaki, T., Shatskiy, A., Katsura, T., 2009. The effect of water on the electrical
516 conductivity of olivine aggregates and its implications for the electrical structure of the upper
517 mantle. *Earth Planet. Sci. Lett.* 288, 291–300.

518 Zhang, B., Yoshino, T., Wu, X.P., Matsuzaki, T., Shan, S., Katsura, T., 2012. Electrical conductivity
519 of enstatite as a function of water content: implications for the electrical structure in the upper
520 mantle. *Earth Planet. Sci. Lett.* 357–358, 11–20.

521 Zhang, B., Zhao, C., Ge, J., Yoshino, T., 2019. Electrical conductivity of omphacite as a function of
522 water content and implications for high conductivity anomalies in the Dabie-Sulu UHPM belts
523 and Tibet. *J. Geophys. Res.* 124, 12523–12536.

524 Zhao, C., Yoshino, T., 2016. Electrical conductivity of mantle clinopyroxene as a function of water
525 content and its implication on electrical structure of uppermost mantle. *Earth Planet. Sci. Lett.*

526 447, 1-9.

527 **Figure captions**

528 **Fig. 1** Representative FTIR spectra of annealed omphacite and garnet. (a) polarized
529 spectra of omphacite along three orthogonal directions of each grain (X' , Y' and Z'), and
530 (b) unpolarized spectra of garnet from different grains. The omp2 and grt2 spectra were
531 reproduced from Liu et al. (2019). Spectra were normalized to 1 cm thickness and
532 vertically offset.

533 **Fig. 2** Representative complex spectra of (a) omphacite (B260) and (b) garnet (B256).
534 Z'/Z'' is the real/imaginary part of complex impedance, and frequency decreases along
535 the Z' axis from left (1 MHz) to right (1 Hz). An equivalent circuit of a single R -CPE,
536 a resistor (R) and a constant phase element (CPE) in parallel, was used to fit the high-
537 frequency arc. Tail and data scatter at low frequency were due to electrode effects that
538 did not affect sample lattice resistance measurements. Number close to each spectrum
539 is temperature ($^{\circ}\text{C}$), and inset in (a) shows spectra at 600-700 $^{\circ}\text{C}$.

540 **Fig. 3** Measured conductivity of (a) omphacite and (b) garnet at 1-2.5 GPa and 250-
541 850 $^{\circ}\text{C}$. The run at 2 GPa was marked, and lines are linear fittings to measured data of
542 each sample (with H_2O contents labeled) by Eq. (1). Symbols around each line are from
543 the same sample (different symbols for different cycles). Samples omp2 and grt2 were
544 from Liu et al. (2019). Uncertainty is usually smaller than/comparable to symbol sizes.
545 Data sources: assembly background, Yang et al. (2011); Z19, synthetic omphacites in
546 Zhang et al. (2019) at 3 GPa (0% FeO and 280 ppm H_2O and 5.81% FeO and 420 ppm
547 H_2O , with H_2O contents recalculated (see text)); Y12, augite in Yang and McCammon
548 (2012) at 1 GPa (8.31% FeO and 75 ppm H_2O); D09, pyrope in Dai and Karato (2009)
549 at 8 GPa (7.42% FeO and 160 ppm H_2O , with H_2O content not recalculated owing to
550 the different OH bands).

551 **Fig. 4** Modeled conductivity of (a) omphacite and (b) garnet at various FeO and H_2O

552 contents. Colored solid lines were made using Eq. (2), and dashed and dotted grey lines
553 were plotted using Eq. (3) for the bottom and top boundaries of FeO content (omp1 and
554 omp3: see text), respectively. H₂O contents of 100, 200 and 400 ppm in omphacite and
555 20, 40 and 80 ppm in garnet at equilibrium OH partitioning were assumed (see text).

556 **Fig. 5** Electrical conductivity of eclogites with different modal composition and Fe
557 and H₂O contents. (a) omp-rich (65 vol.% omp + 35 vol.% grt) eclogite, (b) grt-rich (35
558 vol.% omp + 65 vol.% grt) eclogite, and (c) a typical conductivity-temperature structure
559 along subduction zones (modified after McGary et al. (2014): note that some reference
560 resistivities were imposed in their starting inversion model: see text). Modeling in (a,
561 b) was conducted with the mineral data in Fig. 4 and Eq. (4): blue, red and green colors
562 highlight the different FeO contents, omp1 + grt1, omp2 + grt2 and omp3 + grt3 (with
563 labels on the right side), and star symbols denote different OH contents in the minerals.
564 Horizontal/vertical shadows in (a, b) show the conductivity/temperature range of the
565 subducting crust at ~70-120 km depth in (c).

566 Table 1 Composition of the starting omphacite and garnet (by wt.%)

	SiO ₂	TiO ₂	Al ₂ O ₃	FeO	MnO	MgO	CaO	Na ₂ O	K ₂ O	Total
omp1	56.84	0.03	9.59	1.64	0.02	10.57	15.39	5.72	0.01	99.81
	<i>0.42</i>	<i>0.02</i>	<i>0.07</i>	<i>0.03</i>	<i>0.01</i>	<i>0.30</i>	<i>0.09</i>	<i>0.03</i>	<i>0.01</i>	
omp2*	55.64	0.07	11.38	4.27	0.02	8.44	12.98	7.31	<0.01	100.11
	<i>0.16</i>	<i>0.03</i>	<i>0.35</i>	<i>0.28</i>	<i>0.02</i>	<i>0.17</i>	<i>0.40</i>	<i>0.24</i>	<i><0.01</i>	
omp3	55.37	0.05	7.87	7.92	0.04	8.39	13.54	6.64	<0.01	99.82
	<i>0.26</i>	<i>0.01</i>	<i>0.08</i>	<i>0.15</i>	<i>0.04</i>	<i>0.03</i>	<i>0.08</i>	<i>0.16</i>	<i><0.01</i>	
grt1	39.48	0.05	22.22	15.40	0.29	9.33	12.24	<0.01	<0.01	99.01
	<i>0.15</i>	<i>0.03</i>	<i>0.07</i>	<i>0.17</i>	<i>0.01</i>	<i>0.18</i>	<i>0.19</i>	<i><0.01</i>	<i><0.01</i>	
grt2*	37.64	0.03	22.73	26.55	0.74	6.81	5.63	0.03	<0.01	100.16
	<i>0.20</i>	<i>0.02</i>	<i>0.12</i>	<i>0.36</i>	<i>0.08</i>	<i>0.17</i>	<i>0.32</i>	<i>0.02</i>	<i><0.01</i>	
grt3	37.49	0.07	21.63	26.58	0.14	5.02	8.79	0.04	<0.01	99.76
	<i>0.15</i>	<i>0.04</i>	<i>0.10</i>	<i>0.07</i>	<i>0.04</i>	<i>0.10</i>	<i>0.03</i>	<i>0.02</i>	<i><0.01</i>	

567 Assuming all Fe as FeO. Data are the average and standard deviation (italic) by electron

568 microprobe analyses. omp, omphacite; grt, garnet.

569 *: data were reproduced from Liu et al. (2019) (see text).

570 Table 2 Summary of samples and fit parameters

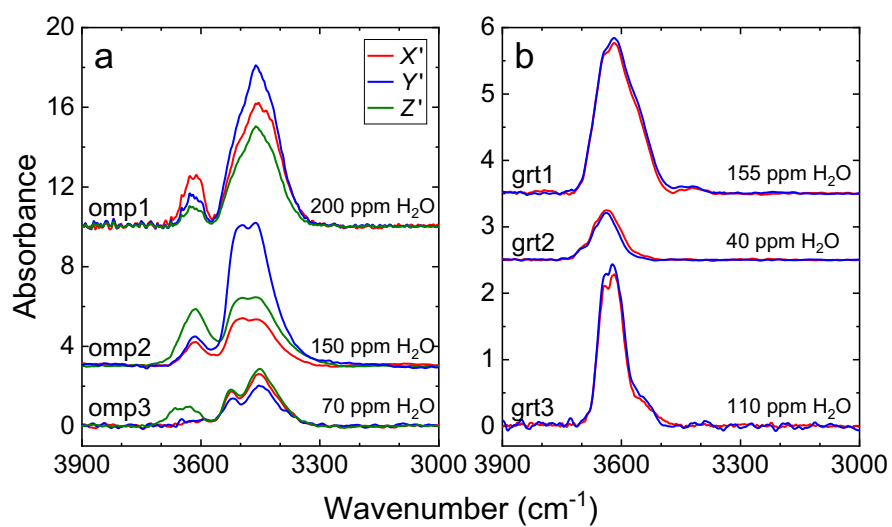
Sample	FeO (wt.%)	<i>P</i> (GPa)	<i>T</i> (°C)	ppm H ₂ O (initial)	ppm H ₂ O (final)	<i>L/S</i> (m ⁻¹)	log ₁₀ (<i>A</i> ₀ (S/m))	ΔH (kJ/mol)
B255 (omp1)	1.64	1	350-700	200	190	288	1.97±0.01	87±2
B185 (omp2)*	4.27	1	350-600	85	80	290	1.38±0.24	84±4
B149 (omp2)*	4.27	1	350-600	150	160	216	1.52±0.14	82±2
B145 (omp2)*	4.27	1	350-650	290	300	269	1.75±0.12	81±2
B260 (omp3)	7.92	1	250-700	70	70	280	1.21±0.07	64±1
B261 (omp3)	7.92	2.5	250-700	70	65	285	1.45±0.04	65±1
B256 (grt1)	15.40	1	350-800	155	150	340	1.89±0.18	93±3
B167 (grt2)*	26.55	1	350-800	40	45	226	1.80±0.17	90±3
B174 (grt2)*	26.55	1	350-800	100	95	245	2.26±0.12	91±2
B267 (grt3)	26.58	1	350-850	110	110	246	2.15±0.13	88±2

571 Water contents are the values prior to (initial) and after (final) conductivity runs, and are rounded to the nearest 5 ppm. *L/S* is the ratio of
 572 sample length to cross-section area (by considering the effective contact between electrodes and sample). FeO contents of the samples are
 573 shown (from Table 1).

574 *: samples were used in Liu et al. (2019) for documenting the water content exponent of 1 in Eq. (2).

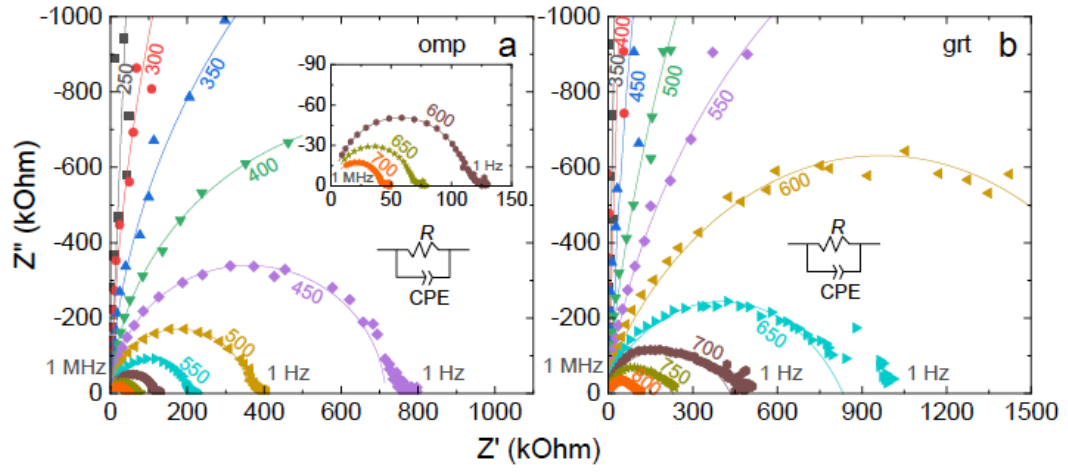
575

Fig. 1



580

Fig. 2



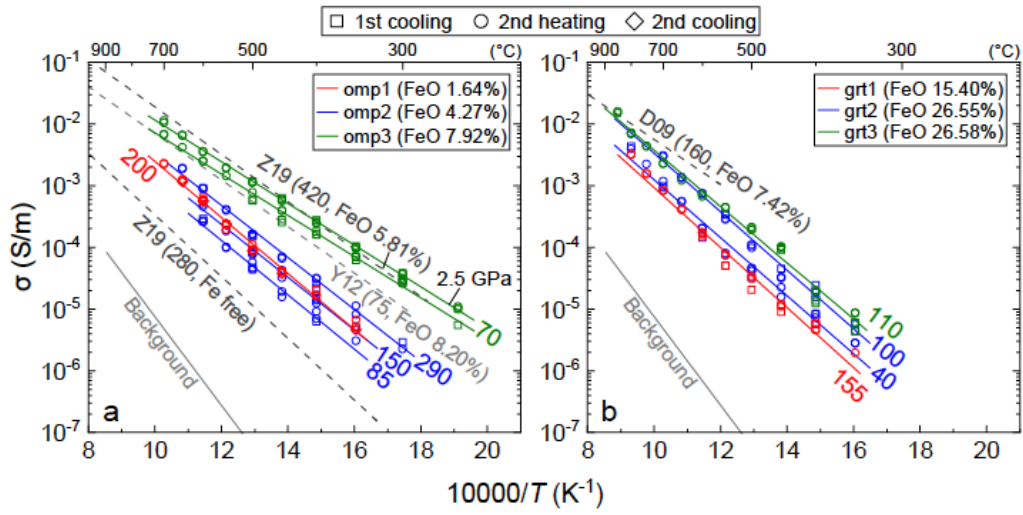
581

582

583

584

Fig. 3

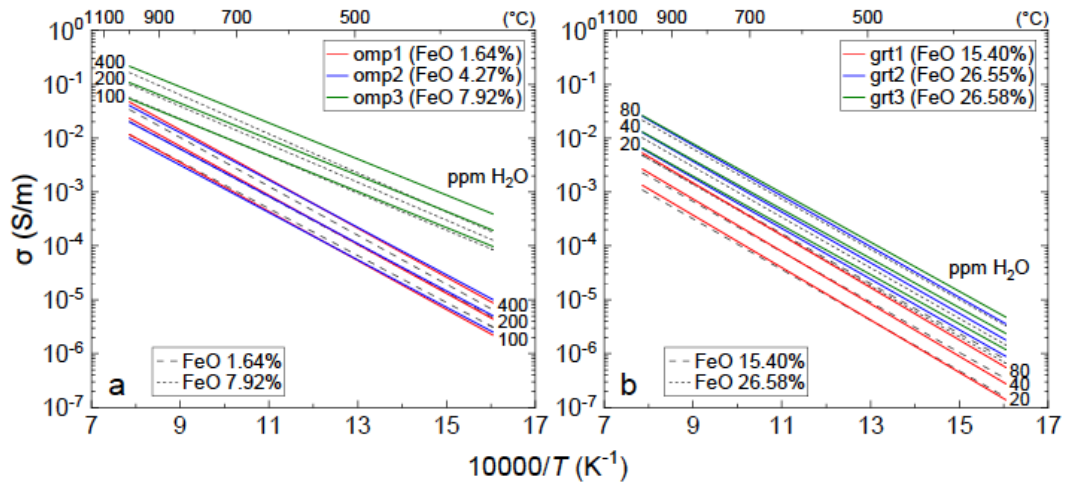


585

586

587

Fig. 4



589

590

591

592

Fig. 5

